Mechanical behaviour at high temperature as induced during welding of a 6xxx series aluminium alloy

Daniel Maisonnette, Didier Bardel, Vincent Robin, Daniel Nélias, Michel Suéry

▶ **To cite this version:**

Daniel Maisonnette, Didier Bardel, Vincent Robin, Daniel Nélias, Michel Suéry. Mechanical behaviour at high temperature as induced during welding of a 6xxx series aluminium alloy. International Journal of Pressure Vessels and Piping, 2017, 149, pp.55-65. 10.1016/j.ijpvp.2016.12.004 . hal-01804248

HAL Id: hal-01804248
https://hal.science/hal-01804248

Submitted on 21 Nov 2023

HAL is a multi-disciplinary open access archive for the deposit and dissemination of scientific research documents, whether they are published or not. The documents may come from teaching and research institutions in France or abroad, or from public or private research centers.

L'archive ouverte pluridisciplinaire **HAL**, est destinée au dépôt et à la diffusion de documents scientifiques de niveau recherche, publiés ou non, émanant des établissements d'enseignement et de recherche français ou étrangers, des laboratoires publics ou privés.

ACCEPTED MANUSCRIPT

Mechanical behaviour at high temperature as induced during welding of a 6xxx series aluminium alloy

D. Maisonnette[a], D. Bardel[a,b,c], V. Robin[c], D. Nelias[a,*], M. Suery[d]

[a] *Univ Lyon, INSA-Lyon, CNRS UMR5259, LaMCoS, F-69621, France*
[b] *Univ Lyon, INSA-Lyon, CNRS UMR5510, MATEIS, F-69621, France*
[c] *AREVA NP, Département d'ingénierie mécanique, Lyon, France*
[d] *Université Grenoble Alpes, SIMaP, CNRS UMR5266, F-38402 Saint Martin d'Hères Cedex, France*

Abstract

Thermal loadings representative of a welding cycle at a point in the Heat Affected Zone (HAZ) of an Electron Beam Welding (EBW) have been reproduced experimentally. It means that the temperature is continously varying, first increasing (during heating) and then decreasing (during cooling) without dwell-time at the highest temperature. Tensile tests have been carried out either during heating or during cooling of the specimen. The mechanical properties of two idealized phases - T6 temper and O temper - have been estimated as a function of temperature. To validate the accuracy of this thermo-mechanical database, a comparison between measured and calculated stress-strain curve is then presented which shows that this approach may be useful to predict the tensile behaviour of this alloy at high temperature whatever the experienced temperature history representative of EBW. Finally, a comparison between numerical and experimental residual stresses is presented for a beam girth weld application.

Keywords: 6061 Aluminium Alloy, Thermomechanical properties, Electron Beam Welding, Stress-strain curves, Yield strength, Finite Element modeling

1. Introduction

The 6061-T6 aluminium alloy (AA) is an age hardenable alloy, it means that its mechanical properties are mainly controlled by the hardening precipitates contained within the material [1]. The optimum mechanical properties in terms of yield strength are gotten after a solution heat treatment followed by a quenching and a tempering treatment at 175° C [2, 3]. The present work focuses on the mechanical properties of this alloy after and during various rapid heat treatments as encountered during electron beam (EB) welding. To achieve this goal the mechanical properties of the AA6061 alloy will be investigated after different temperature histories. This kind of data are necessary for Computational welding Mechanics (CWM)[DB] in order to predict residual stresses and distortions due to welding operations [4, 5, 6, 7]. In this paper, it will be shown that, in a single pass welding process a simple isokinetic model [8] provides a good estimation of the mechanical properties after transient heat treatments when coupled to the work-hardening model proposed in this work. Note that the recently performed simulations of laser welding by [9], friction stir welding [10], laser shot peening [11] and gas metal arc welding [12] require this type of database, as well as additive manufacturing modeling.

The behavior of AA6061 at room temperature – after various thermal histories – has been investigated by Bardel et al. [13]. It shows that the mechanical properties, such as the yield strength, are strongly dependent on the microstructure which is varying with time due to the growth or dissolution of hardening precipitates. It was for example shown that: (i) the mechanical properties diminishe when the maximum temperature reached increases or when the heating rate decreases, (ii) all $\beta'' - \beta'$ hardening precipitates in AA6061-T6 are dissolved at 560° C whatever the heating rate. However, the knowledge of the mechanical properties at room temperature is not sufficient to model accurately a process involving high temperatures and thermal gradients encountered both in space and time during welding or additive manufacturing. The knowledge of mechanical properties at temperature ranging from 20° C and 560° C are required to simulate the welding process. This is the purpose of the present investigation. Note that the solidification or the properties of the melted alloy are not studied here.

In this study, to be as representative as possible of the precipitation state evolution encountered in the HAZ under welding condition and to model the mechanical properties during welding, the thermal loadings applied to specimens will not include dwell time before the beginning of the tensile tests. These experiments include tensile tests at high temperature during either heating or cooling. Results are used to propose non measurable stress-strain curves at various temperatures for the T6 and O states (the latter meaning that all $\beta'' - \beta'$ hardening precipitates are dissolved) for transient heat treatments. These data complete the high strain rate investigation performed by Pickett et al. [4] and Abotula and Chalivendra [14], but also the work of

*daniel.nelias@insa-lyon.fr

Robin *et al.* [15] who applied their model to Electro-Magnetic Forming (EMF). These data will be then used as input for a two-phase thermo-mechanical model and we will demonstrate the good prediction that this model can provide thanks to a confrontation between welding simulations and instrumented experiments (including neutron diffraction).

2. Mechanical testing at high temperature

2.1. Experimental procedure

A home made heating device using Joule effect with continuous current was adapted to a tensile machine to monitor the temperature history during the tensile test by the mean of thermocouples connected to a temperature controller. Here, the specimens are heated to the test temperature (see Fig. 1) and the tensile test starts immediately at a controlled strain rate $\dot{\varepsilon}$=8.10^{-5} s^{-1}. Moreover, an extensometer with ceramic tips, a load cell and a video camera are used to record the local uniaxial strain, the strength and the evolution of the diameter, respectively.

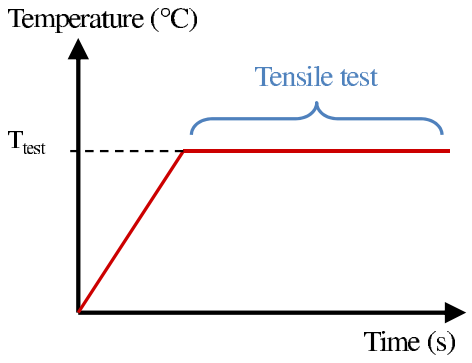

(a)

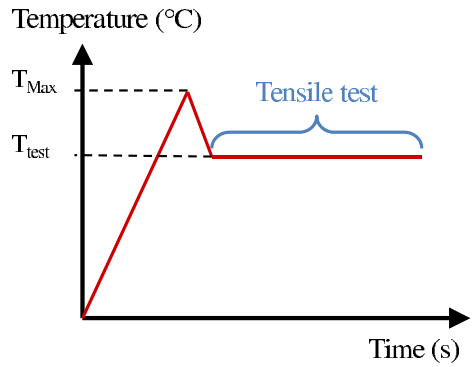

(b)

Figure 1: Tensile test procedure from T6 state: (a) after heating and (b) after overheating and partial cooling.

The first tests have been performed at different temperatures (constant heating rate of r = 15 C/s[DB]) on T6 specimens (this initial microstructural state corresponds to a high density of β'' precipitates [16, 17]). As shown in Fig. 1, since tensile tests have been realized at the desired temperature without dwell, it means that a microstructural degradation (dissolution or growth of precipitates) may occur during the experiments.

A second series of tensile tests has been carried out at various temperatures but with a different heat treatment before the tensile test started. The specimens have been firstly heated at T_{Max} = 560° C (above the solvus close to 530° C [18, 19]) to get the so-called O temper state (all the hardening precipitates are dissolved even without dwell time [2]). Then, thanks to a special design of the machine and the specimens to get fast cooling (above 15° C/s as suggested in [20]), the microstructural state is kept before the tensile test at a given temperature started (see Fig. 1b).

2.2. Post treatment

Material softening can be observed during tensile tests at some specific temperatures. Its occurence can be explained by two phenomena:

- the precipitation state is evolving during the test and the degraded microstructure leads to less hardening.
- in the middle of the specimen a necking can occur and produce a significant decrease of the section compared to the initial one.

To distinguish the microstructural and the mechanical effects the use of true stress and logarithmic strain is needed, instead of engineering starin and stress. To distinguish the softening due to the microstructure and the one due to necking, the stresses that becomes no longer uniaxial are reassessed thanks to the Bridgman factor [21] which takes into account the triaxiality. This factor requires the identification of the specimen radius (noted a) in the necking zone and the radius of the necking contour (noted R). These two radii (see Figs. 2a and 2b) are measured thanks to image recording, which in turns allows to correct the strain-stress curve according to necking with the following equations:

$$F_{\text{Bridgman}} = \frac{1}{(1 + 2R/a)\ln(1 + a/(2R))} \tag{1}$$

Then, the Bridgman stress is calculated in such way:

$$\sigma_{\text{Bridgman}} = F_{\text{Bridgman}} \times \sigma_{\text{Cauchy}} \tag{2}$$

Consequently the remaining softening visible on the strain-bridgman stress curves of Fig. 3 in the next section is only due to microstructural effects.

During the tensile test, the homogeneity of the strain between the ceramic tips allows to get an accurate measurement of the strain. Nevertheless, when necking occurs, the provided strain is affected and the measurements are erroneous. To bypass this problem, the logarithmic strain of Hencky ($\varepsilon_{\log} = \ln\left(\frac{L}{L_0}\right)$) is corrected at the beginning of necking and the definition becomes:

$$\varepsilon_{\log} = \ln\left(\frac{A_0}{A_i}\right) = \ln\left(\frac{{D_0}^2}{{D_i}^2}\right) = 2\ln\left(\frac{D_0}{D_i}\right) \tag{3}$$

where A_0, A_i and D_0, D_i = $2a$ are: the initial/instantaneous cross-section and the initial/instantaneous diameters.

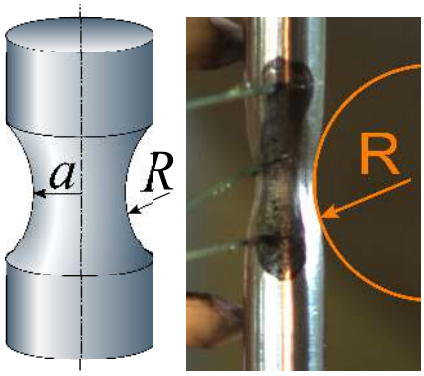

(a) (b)

Figure 2: (a) Necking zone geometry and definition of the radii used for the calculation of the Bridgman factor, (b) example of R measurement.

3. Results

3.1. During heating (from the T6 state)

In Fig. 3 the strain-stress curves obtained at various temperatures ranging from 20 to 560° C are presented. Note that here the effect of the thermal expansion has not been substracted.

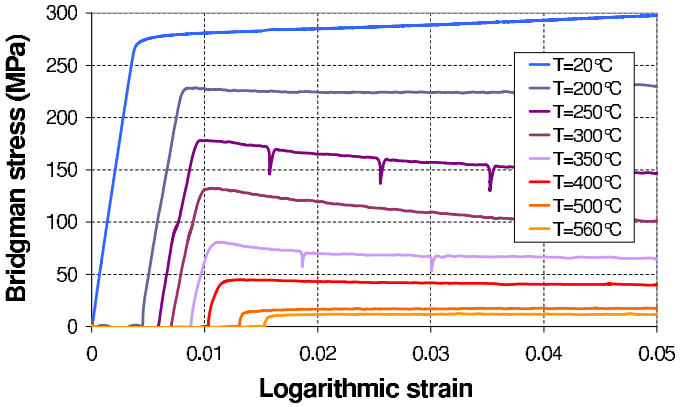

Figure 3: Bridgman stress versus logarithmic strain for various temperatures from T6 state (thermal expansion is not subtracted)

In the T6 state at room temerature a slight hardening is observed while a significant softening is observed for tempeatures ranging between 250 and 400° C. On the light of simulations conducted in [2] this effect is attributed to the dissolution/coasening of the $\beta'' - \beta'$ hardening precipitates. Such behaviour is not commonly reported in the literature. Nevertheless, this kind of softening has already been reported in [22] for an AA6056 alloy in the T4 temper state (under aged condition). Note that here, the hardening precipitates are already dissolved when a temperature of $T = 500°$ C is reached (see results in [2]). Consequently, no softening is encountered during the tensile test between $T = 500°$ C and 560° C because the microstructural state is already stabilized before the mechanical sollicitation).[DB]

The yield strength σ_y can be distinctly identified on these curves[DB] and its evolution is then reported in Fig. 4a. Its value is σ_y=278 MPa at room temperature (T6 state), it decreases to 228 MPa at $T = 200°$ C and drops to 9.7 MPa at $T = 560°$ C. A comparison with the experimental data from the literature [23] is also provided. In their experiments tensile tests have started after a dwell time of 30 min (however the heating rate there is not known). It is therefore consistent to find here higher yield strength than in [23] at temperatures above 250° C. Note also that the yield strength obtained at R.T. and at 200° C are identical.

Moreover, in Fig. 4b, the evolution of the Young modulus is plotted and compared to the results obtained by [24]. Note that during their experimental campaign a low heating rate – close 0.08°C/s – was employed. However that should not have a significant impact since the elastic properties of age hardening aluminium alloys are not depending on the precipitation state[DB]. Between room temperature and $T = 200°$ C there is no evolution, but a significant and almost linear decrease from $E = 68$ GPa at $T = 200°$ C to $E = 26.7$ GPa at $T = 560°$ C can be observed.

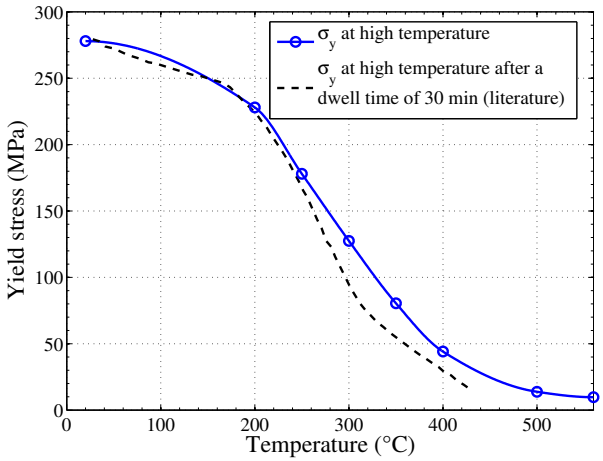

(a)

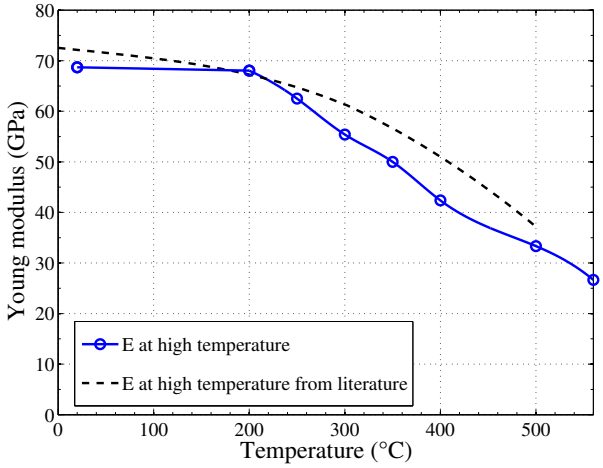

(b)

Figure 4: Evolution of (a) the yield strength σ_y and (b) the Young modulus versus test temperature from T6 state. Experimental data from the literature are taken from [23] and [24], respectively.

3.2. During cooling (from the O state)

The strain-stress curves at temperatures ranging from R.T. to 560° C are presented In Fig. 5, after the O treatment presented in Fig. 1b. These results are of interest since they represent what happens during cooling for hardening precipitate alloys. One may notice a significant hardening of the material that occurs during the tensile tests at R.T. and at 200° C. To the authors' knowledge such data has not yet been published for AA6xxx series. The explanation is provided next.

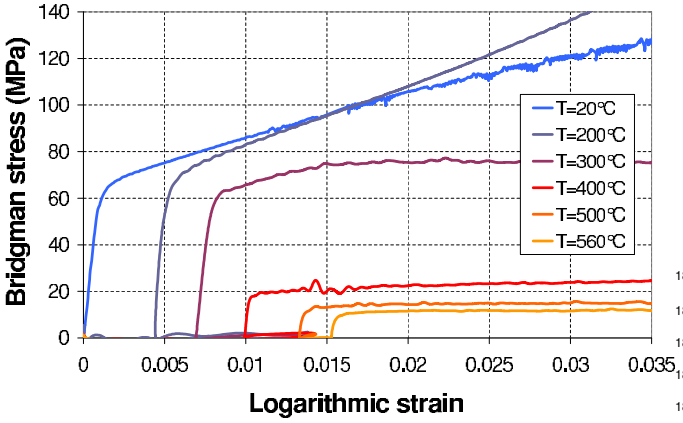

Figure 5: Bridgman stress versus logarithmic strain for various temperatures from O state (thermal expansion is not subtracted)

In the O state (i.e. at $T = 560°$ C: all hardening precipitates are dissolved) the results are naturally similar to those reported in the previous section. However, conversely to the previous results, no softening is reported for all the other curves in the plastic domain and a large work hardening appear from $T = 200°$ C. Indeed, this temperature is close to the tempering one and in these conditions the 0 state rapidly evolves [2] because many hardening precipitates nucleate during the tensile test and harden the alloy throughout the test. Note that, in these tests, the fracture comes much faster: the ductility is here around 4 % compared to a range of 20-80 % for the previous tests.

For these experiments, the evolution of the yield strength is plotted in Fig. 6. Between $T = 560°$ C and 400° C the temperature is still high and no significant nucleation is produced: the yield strength slightly increases when the test temperature decreases. Below 400° C, a sharp increase of the yield strength is produced thanks to the progressive formation of $\beta'' - \beta'$ hardening precipitates during this tensile test at low strain rate. When the temperature is still decreasing from 300° C to room temperature the nucleation rate (see [2] for details) increases as well as the yield strength. It should be noted that the yield strength, which ranges from $\sigma_y = 9.7$ MPa at $T = 560°$ C to $\sigma_y = 62$ MPa at $T = 200°$ C when the alloy is tested from the O temper state, is significantly lower than that measured during heating e.g. from the T6 temper state (278 MPa at 200° C, see Fig. 3).

3.3. Additionnal tests at $T = 200°$ C and $T = 300°$ C

In this subsection some additional tests are presented to highlight some of the previous results.

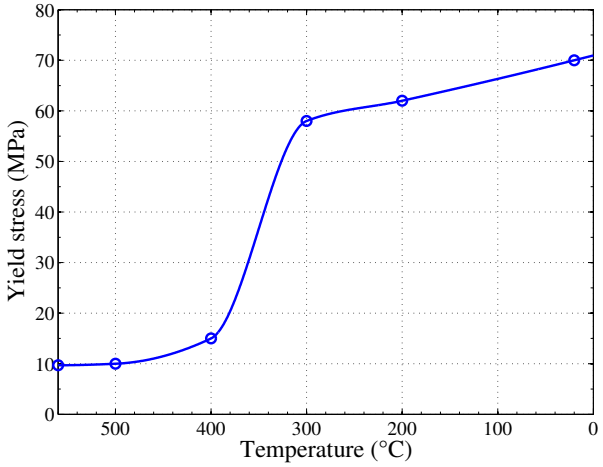

Figure 6: Yield strength versus test temperature from O state (during cooling)

Tests at $T = 200°$ C

To investigate the influence of the strain rate at $T = 200°$ C, another tensile test has been performed at $\dot{\varepsilon} = 4.10^{-4}$ s $^{-1}$ after preheating at $T_{Max} = 560°$ C. The strain-stress curve is plotted in Fig. 7 along with the results of the previous tests ($\dot{\varepsilon} = 8.10^{-5}$ s $^{-1}$) from T6 and O temper state already presented in the previous sections. It is interesting to observe that the hardening observed at high strain rate is weaker than the hardening obtained for the same curve preheating at $T_{Max} = 560°$ C but with a low strain rate. This observation is consistent because precipitates have less time to nucleate and then to improve the mechanical properties of the alloy for a fast heating rate.[DB]

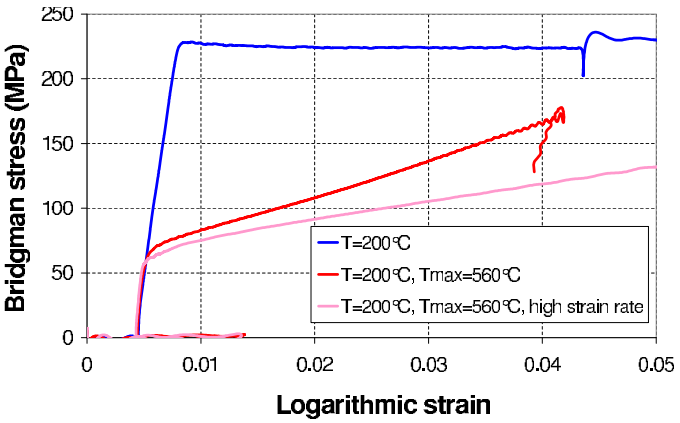

Figure 7: Strain rate effect on stress-strain curves at $T = 200°$ C for the O state compared to the T6 one (Thermal expansion is not subtracted)

Tests at $T = 300°$ C from T6

In this subsection the impact of a dwell time before the tensile test starts is investigated. An additional tensile test at $T = 300°$ C was performed from a T6 state but after a dwell time of 20 min (duration of one test) at the test temperature. The corresponding curve is plotted in gray in Fig. 8 and confronted with the previous results obtained without dwell (as in Fig. 3). One may notice a significant difference: the dwell time

is sufficiently long to permit a stabilization of the precipitation state, finally no softening is observed during the test.

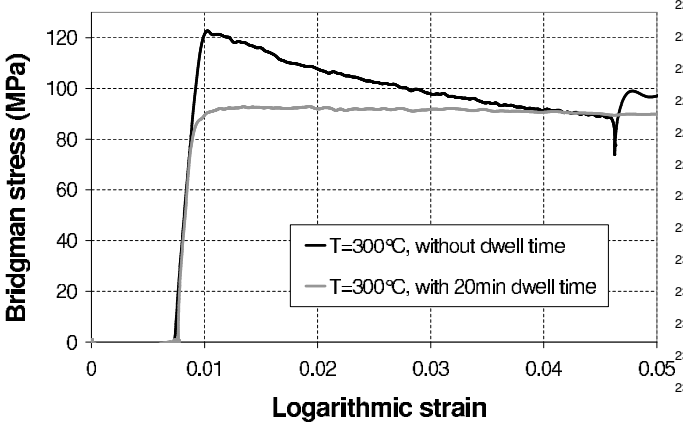

Figure 8: Stress-strain curve at $T = 300°$ C for T6 state with and without dwell time (Thermal expansion is not subtracted)

Effect of pre-heating

Another interesting comparison consists to observe the effect of the pre-heating on the elastic-plastic behaviour. Thus, in Fig. 9, three tests performed at $T = 300°$ C are presented: (i) a first test where the initial state is T6 (as in Fig. 3), (ii) a second one from the O state (i.e. previously heated at $T = 560°$ C) as in Fig. 5 and (iii) a new test similar to the second one but where the maximum temperature is $T = 400°$ C only.

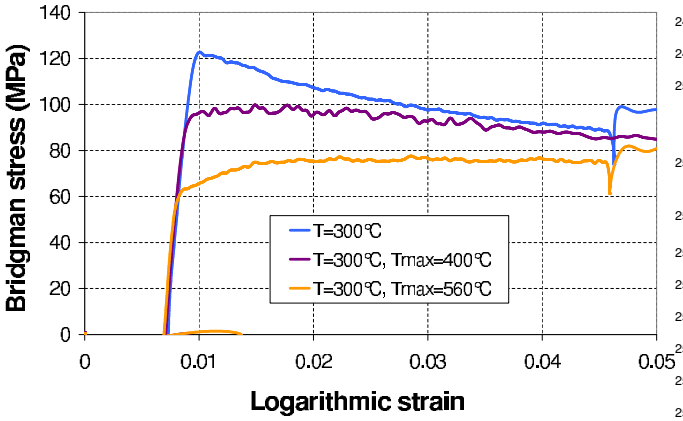

Figure 9: Strain-stress curve at $T = 300°$ C for various maximum pre-heating temperatures (Thermal expansion is not subtracted)

The specimen which has undergone pre-heating at $T_{\text{Max}} = 560°$ C is the only one that does not exhibit softening because all the hardening precipitates have been dissolved at the beginning of the test. On the other hand, a non negligible quantity of hardening precipitates subsists for the two others as demonstrated in [2]. This explain why the yield strength is higher and why a softening is present due to their dissolution during the test.

3.4. Discussion: comparison with published data

Usually, for this kind of age hardening alloys, tensile tests are performed after a long dwell time at the test temperature in order to stabilize the material microstructure. However, the final goal of this work is to provide experimental data for welding and additive manufacturing applications where the kinetics are very fast. So it requires new database where no dwell time are involved during the thermo-mechanical treatment. It means that the microstructure can evolve significantly during the tensile test and the data are more consistent with the loadings undergone during welding or additive manufacturing. To the best of the authors' knowledge, little data in the literature are representative of this type of processes for AA6xxx alloys.

To check the results presented above the evolution of yield strength given in [23] after a dwell time of 30 min was confronted with our results in Fig. 4a. The differences can be explained in light of recent Small Angle Neutron Scattering (SANS) and thermodynamical simulations reported in [2]:

- when $T < 250°$ C the results are similar because the temperature and the dwell time are too low to significantly impact the precipitation state.
- above 250° C, a microstructural evolution (coarsening/dissolution) starts to take place at the beginning of our test. Furthermore, the dwell used in [23] amplifies this microstructural evolution and the lower values obtained at the beginning of the tensile test are the consequence of a larger degradation of the initial T6 state.

Concerning the Young modulus, the results given by Sharma et al. [24] and our are close but not similar. These difference are probably due to the chemical composition which is slightly different (they studied a Al6061 alloy composites). In addition the test conditions, that are not provided in their paper, differ also probably.

4. Phenomenological model

4.1. Introduction

In order to get a constitutive law for thermo-mechanical loadings, as for welding applications, a phenomenological model is proposed in this section. The objective of this model is to reproduce the behaviour of this age hardening alloy, initially in the T6 state, from room to solidus temperatures, especially the hardening or the softening that was highlighted in the previous section (e.g. from 200 to 400° C). The metallurgical model proposed in this section is a coupling between a microstructural one and a work hardening model, it aims to predict the mechanical behaviour during a single pass welding process where the hardening precipitates are dissolved.

To simulate the evolution of the precipitation state for the AA6xxx series, multi-class precipitation models are good candidates [8, 25, 26]. Recently, the authors successfully coupled this physical approach to strengthening models to predict, at room temperature, the monotonic and cyclic behaviour of this Al 6061 alloy previously subjected to complex heat treatments [2, 3]. Nevertheless, the physical understanding of the precipitation-hardening coupling during thermo-mechanical loadings is not yet well understood. However, recent studies of the authors on AA6061-T6 [2] have shown that

for this kind of transient heat treatments, the main mechanism is the decrease of the density of precipitates by pure dissolution or coarsening. Thus, a phenomenological microstructural approach composed by a hard and a soft phase is employed where the evolution of the soft one (in the initial T6 state the proportion is 0) is deduced thanks to the isokinetic model proposed by Myhr et al. [27]. In addition to its simplicity, the chemistry of the alloy is not taken into account, it allows a relative general application for the 6xxx series.

Knowing the proportion of these two phases:

- the first represents the maximal hardening (the T6 state, here called hard phase) ;
- the other represents the minimal hardening (the O state, here called soft phase).

a law of mixtures is employed in the mechanical part of the model to provide the strength of the alloy for each temperature. However, this methodology requires the knowledge of the behaviour of the hard and the soft phases at each temperature without the microstructural effect which is already provided by the isokinetic simulation [27]. These behaviours are non measurable because the precipitation state evolves continuously during each experiment. Thereby, the purpose of this investigation is to determine, thanks to an inverse method, the stress-strain cuves of these soft and hard phases with temperature. For that, a dedicaced Finite Element (FE) model is used to reproduces the experients and to identify these curves. Note that the identification of the mechanical behaviour at room temperature of each of these phases does not require additional effort since it corresponds to what has been measured from T6 and O temper states, as quickly presented above and also in greater details in [28].

4.2. Thermo-electrical, microstructural and mechanical simulations of the tensile tests

To best fit with experiments the simulation of tensile tests is needed. These simulations consists in two uncoupled steps:

- a electro-kinetic or thermo-electrical (TE) analysis, calibrated thanks to the thermocouple measurements, that provides as input of the mechanical analysis the heat treatment and temperature gradient in the specimen. These data are needed in order to accurately reproduce the mechanical behaviour. The resulting thermal history allows to compute, at each time step, the proportion of the soft and hard phases in the specimen.
- Then a microstructural and mechanical (MM) analysis is performed to estimate at each integration point the resulting constitutive law and then simulate the tensile test.

Finally, the resulting stress-strain curves are confronted to the experimental ones to identify the behaviour of the hard and soft phases (that are not known during a temperature treatment, just at room temperature) for each thermal treatment.

4.2.1. Presentation of the model

Electro-thermal analysis.

To reproduce the Joule heating used to heat the specimen, an electro-thermal analysis is performed with the commercial software Sysweld® [29] from the heat equation:

$$\mathrm{div}\left(\lambda^t \overrightarrow{\mathrm{grad}T}\right) + P = dc_p \frac{\partial T}{\partial t} \tag{4}$$

where T, t, λ^t ($\mathrm{W.m^{-1}.K^{-1}}$), P ($\mathrm{W.m^{-3}}$), d ($\mathrm{kg.m^{-3}}$), and c_p ($\mathrm{J.kg^{-1}.K^{-1}}$) are respectively the temperature, time, thermal conductivity, the energy produced in the material per unit volume, the density and the specific heat.

In this thermal problem, the energy P corresponds to the electrical energy defined by [30] (Q is a potential volume heat source added to the electrical one):

$$P = \overrightarrow{\mathrm{grad}V}.\left(\vec{J}\right) + Q = \overrightarrow{\mathrm{grad}V}.\left(\overline{\sigma}(T)\overrightarrow{\mathrm{grad}V}\right) + Q \tag{5}$$

where V, $\overline{\sigma}(T)$ and $\vec{J}$ are the electrical potential, the electrical conductivity tensor, and the current flux computed at each node through the electro-kinetic equation $\mathrm{div}\vec{J} = 0$.

The equation solved by Sysweld® [29] assumes that the thermal conductivity and the specific heat (now written as function of the enthalpy H: $c_p = \partial H/\partial T$) of each phase proportion p_i may differ from one phase to another. In this case the total enthalpy and conductivity become: $H = \sum_{\mathrm{phases}} p_i H_i$ and $\lambda^t = \sum_{\mathrm{phases}} p_i \overline{\lambda_i^t}$. Finally, by remplacing $dc_p \frac{\partial T}{\partial t}$ as function of $d\dot{H}$:

$$d\dot{H} = \sum_{\mathrm{phases}} d_i H_i \frac{\partial p_i}{\partial t} + \sum_{\mathrm{phases}} d_i p_i \frac{\partial H_i}{\partial t} \tag{6}$$

we get the solution of this thermo-electrical problem:

$$\begin{aligned} &\sum_{\mathrm{phases}} d_i(T) H_i \frac{\partial p_i}{\partial t} + \sum_{\mathrm{phases}} d_i(T) p_i \frac{\partial H_i}{\partial t} \ldots \\ &-\mathrm{div}\left(\textstyle\sum_{\mathrm{phases}} p_i \overline{\lambda_i^t}(T)\overrightarrow{\mathrm{grad}T}\right)\ldots \\ &\qquad -\overrightarrow{\mathrm{grad}V}.\left(\overline{\sigma}(T)\overrightarrow{\mathrm{grad}V}\right) - Q = 0 \end{aligned} \tag{7}$$

Calculation of phase proportion.

The thermal analyis takes into account the microstructural evolution of the alloy through the hard and the soft phase proportions, namely p_1 and p_2 (with $p_1 + p_2 = 1$ and $p_1 = 1$ for the T6 state and $p_2 = 1$ for the O state). The computations presented in this section aim to describe the kinetic of this process thanks to the Myhr et al. [27] isokinetic model. Indeed, it was shown that the dissolution rate of the hard phase is defined by:

$$\dot{p}_2 = \frac{n \times {p_2}^{\left(1-\frac{1}{n}\right)}}{t^*} \tag{8}$$

with n and t^* equal to:

$$n = 0,5 - a{p_2}^b \tag{9}$$

$$t^* = t^*_{r_1} \exp\left[\left(\frac{Q_s}{nR} + \frac{Q_d}{R}\right)\left(\frac{1}{T} - \frac{1}{T_{r_1}}\right)\right] \tag{10}$$

in these equations a, b are two constants and Q_s, Q_d, $t^*_{r_1}$ are the enthalpy of dissolution, the activation energy of the diffusion and the time needed to reach a total dissolution at the temperature T_{r_1}. These parameters have to be fitted on microstructural evolutions. Here, the values provided by Hirose et al. [31] will be chosen (cf. table 1) because they have already provided good hardness predictions in weld joint [31].

Table 1: Numerical values of parameters employed in the microstructural model

Parameters	Numerical values
a	0.394
b	0.107
Q_s	30 kJ/mol
Q_d	130 kJ/mol
$t^*_{r_1}$	600 s
T_{r_1}	375° C

Mesh, properties and boundary conditions. The FE model used here is axisymmetrical with a fine mesh (0.16×0.3 mm^2) in the middle of the specimen where high gradients are involved and because all data will be measured there. 2800 quadrilateral linear elements (called Q4 in Sysweld®) are employed to mesh the whole test specimen.

Several boundary conditions are needed to solve eq. 8, they are schematically drawn in Fig. 10. First of all, to compute $\vec{J}$ electrical boundary conditions are needed:

$$\overline{\sigma}(T).\overrightarrow{\text{grad}V}.\vec{n} = j(V) \quad (11)$$

$$V = V_0 \quad (12)$$

here, V_0 is the imposed electrical potential and $j(V)$ the imposed current density which is located at the beginning and at the end of the cylindrical area of the specimen (red arrows in Fig. 10). The current intensity is close to that measured during the heating of the specimens during tensile tests but some adjustments are required to obtain the desired thermal loading.

Concerning the thermal boundary conditions, a temperature of 12° C during the whole simulation is chosen in the specimen heads as during the experiments (the clamping system is water-cooled). Then, an air-specimen heat transfer coefficient is chosen equal to 50×10^{-6} W.mm^{-2}.K^{-1}.

The material properties, the electrical conductivity, the specific heat, the density and the thermal conductivity (both are temperature dependant) are taken from the litterature [32, 33]: $\rho = 3.7\times10^{-8}$ Ω.m ; $C_p = 896$ J/(Kg.K) ; $d = 2700$ and $d = 2617$ Kg/m^3 (0 and 400°C) ; $K = 150$, $K = 184$ and $K = 173$ W(m.K) (0, 350 and 540°C).

4.2.2. Results of the thermo-microstructural analysis

Note that heat exchange by radiation is assumed to be negligible compared to heat transfer by conduction and convection, and then is not included here for sake of simplicity. Then, in this section, two examples of microstructural results are presented:

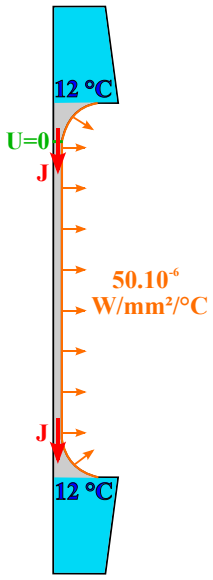

Figure 10: Schematic illustration of the electro-kinetic and thermal boundary conditions

- for a heating up to $T = 300°$ C from T6 state which results in the most pronounced softening,
- another one up to $T = 500°$ C where all the hardening precipitates ($\beta'' - \beta'$) should be dissolved [2].

The evolution of temperature at the middle of the specimen and during the heating up to 300° C is plotted in Fig. 11a along with the phase proportions of the soft and hard phases. As demonstrated in the experimental section, even before the beginning of the tensile test, a very fast dissolution of the hard phase occurs and keeps going during the tensile test. This result again justifies why the heating phase is of interest and why no dwell time must be used to characterize the mechanical behaviour of these alloys.

Similar results are presented in Fig. 11b for the heating up to 500° C. Here, conversely to the previous example, a complete dissolution is reached before the beginning of the tensile test. More precisely, the hard phase is completely dissolved when 492° C is reached, it confirms that a stable state is obtained at 500° C prior to the mechanical loading. It explains why there is no softening in this test.

4.3. Mechanical modeling of tensile tests

In this section a mechanical model, which describes the elasto-plastic behaviour of the hard and the soft phases at each temperature, is coupled to the thermo-microstructural analysis presented in the previous section.

4.3.1. Description of the mechanical model

In this analysis, the constitutive law used at each integration is determined thanks to a mixture law given by:

$$Y(\epsilon, T) = p_2 \times Y_{\text{O}}(\epsilon, T) + (1 - p_2) \times Y_{\text{T6}}(\epsilon, T) \quad (13)$$

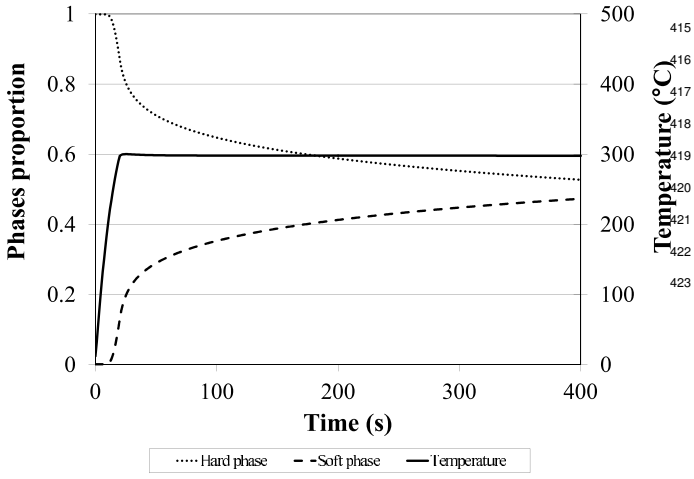

(a)

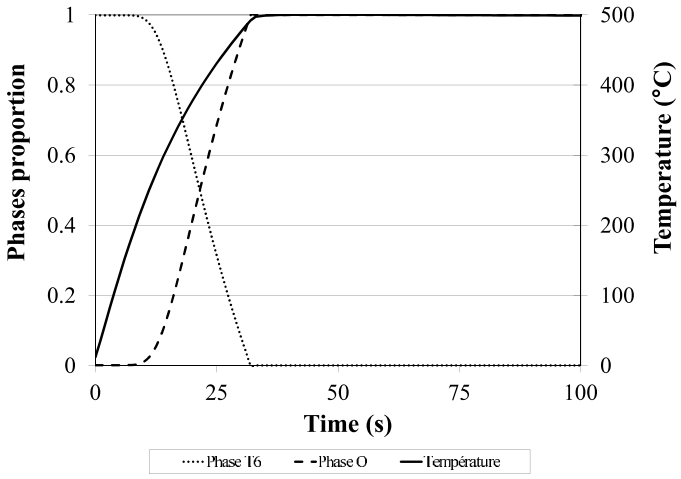

(b)

Figure 11: Evolution of temperature and phase proportion (a) at $T = 300°$ C (b) at $T = 500°$ C

where $Y(\epsilon, T)$ is the resulting strength of the alloy computed thanks to the proportion of the hard (p_1) and soft phases (p_2) and the corresponding stress-strain curve at each test temperature. The overall problem consists in the determination of the stress-strain curves of the phases Y_O/Y_{T6} for each temperature.

4.3.2. Mechanical modeling of tensile tests at high temperature

The mechanical analysis can be thus started by moving the specimen heads according to the strain (including the thermal expension) and strain rate monitored experimentally. The resulting strain-stress curve computed for each test temperature is confronted to the experimental ones.

Note that in eq. 13 the hard and soft phase laws are not known at high temperature and they cannot be deduced by means of experimentations because of the microstructural evolution during the test. Thereby, they are determined thanks to an inverse method in order to reproduce the experimental behaviour of the sample. An initial guess for the behaviour laws of the two phases used as input data for the mechanical model and is then incrementally changed until a good agreement between the simulated and experimental tensile curves is found. The time step is also adjusted to have a good numerical stability. The results of this inverse method is shown in Fig. 12 for the test where $T = 300°$ C and $T = 500°$ C: the experimental softening is well represented as the nill work hardening. The numerical stress values and logarithmic strains are plotted as for experiments: the stresses are measured on the specimen heads and logarithmic strains are deduced from the displacements at the positions where the extensometer tips are located.

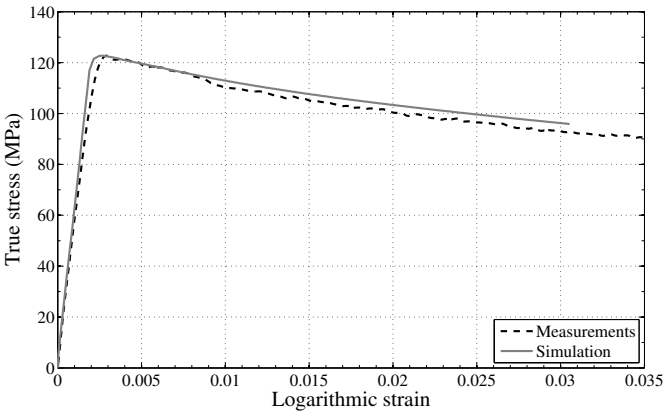

(a)

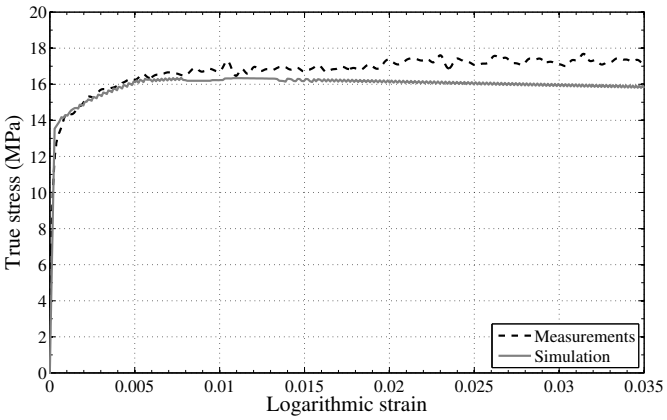

(b)

Figure 12: Comparison of tensile curves obtained by experimental and numerical investigations (a) at $T = 300°$ C (b) at $T = 500°$ C

The constitutive laws of the hard and soft phases deduced thanks to the inverse method are presented in Fig. 13. It is important to emphasize that the hardening laws of both phases at the various temperatures correspond to the behaviour that would have the two phases T6 and O if they were measurable. For most of the curve, a low work hardening is needed for each phase to reproduce the resulting softening experimentally observed because of the microstructural transformation that is still active during the test. These results are the final goal of this study because thanks to the mixture law eq. 13 they can be used as input data for thermo-mechanical simulations of structures made of AA6xxx-T6 series.

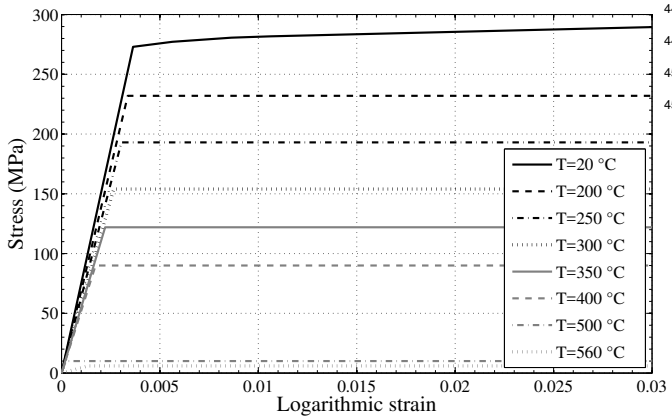

(a)

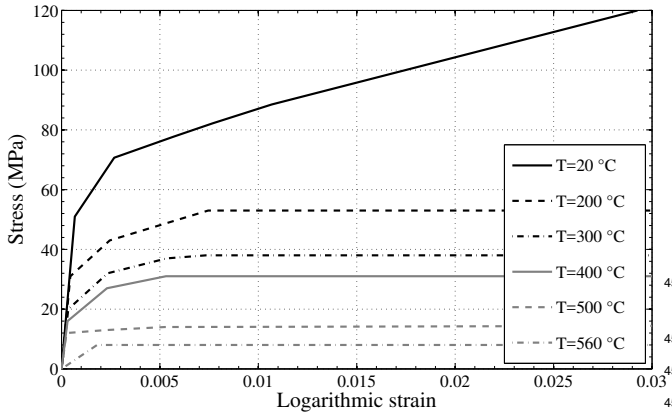

(b)

Figure 13: Constitutive laws obtained by inverse method at various temperatures (a) for the hard phase (b) and for the soft phase

4.3.3. *Predictive ability: mechanical modeling of tensile tests at room temperature*

Our microstructural-mechanical model was built to determine the constitutive law at medium and high temperature for a 6061-T6 alloy. This phenomenological model could also provides good results at room temprature considering a mixture of the hard and soft phases (cf. Fig. 14).

A thermal loading composed by a linear heating (rate r = 15 C/s[DB]) up to a maximum T = 400° C and followed by an air cooling stage was simulated. For transient heat treatment, the thermo-microstructural simulation provides a proportion of hard phase with p_1 = 0.37. The resulting stress-strain curve is compared in Fig. 14 with an experimental one given by a previous work of the authors [28]. We can see that the general trends are well reproduced by this comprehensive two phase model, except in the beginning of the plastic domain.

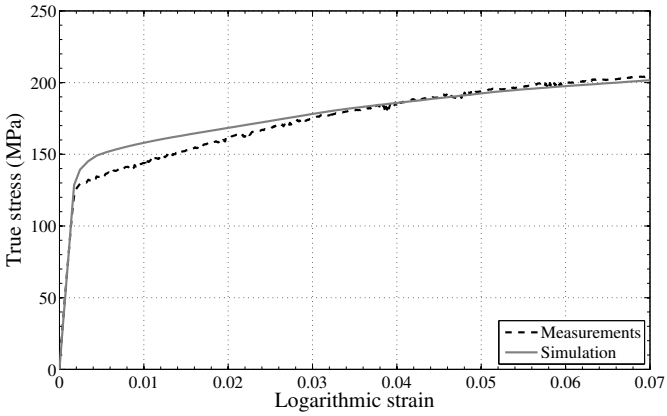

Figure 14: Confrontation between experimental and numerical curves during a tensile test performed at room temperature after a linear heating (rate r = 15 C/s[DB]) up to T = 400° C.

5. FE simulation of electron beam girth weld

In this section, to evaluate the capabilities of our metallurgical model we will confront residual stresses data measured in a girth weld to the corresponding finite element simulation. Note that the calibration of thermal finite element model is not described here because it is similar to previous work [9]: only the calculation steps will be recalled in the first subsection.

5.1. *Computational Welding Mechanics*

Welding issues such as weldability, distortions and residual stresses can be solved by mathematical modeling using Finite Element Analysis (FEA) to compute coupled transient nonlinear problems. This activity refers to Computational Welding Mechanics (CWM) which has become a decision-making tool for welding as well as mechanical engineers [7, 34]. The interactions between heat transfer, metallurgy and mechanics have to be taken into account. Strong coupling is performed to solve thermo-metallurgical part and weak coupling is sufficient to predict mechanical states. Strong coupling means that temperatures and phase proportions are solved in the same set

of equations unlike weak coupling which only needs thermo-metallurgical results as input data.

The heat transfer analysis rests upon the solution of the classical heat equation with appropriate boundary conditions [35]. It is computed on a three-dimensional model in order to properly reproduce the thermal cycles in the heat-affected region. The shape of the heat sources and the input energy are fitted to experimental data (i.e. recording of thermocouples and the dimensions of the weld pool and the heat affected zone obtained from macrograph transversal cuts). The heat input Q is represented by a heat flux distribution. Electron beam welding vaporizes the material and requires a specific shape for heat input distribution. A gaussian volume heat source is used to model such processes. The larger molten zones observed at the top and bottom of the plate is obtained by the mean of two gaussian surface heat sources and allow to get the shape provided by the macrographs (see fig. 15).

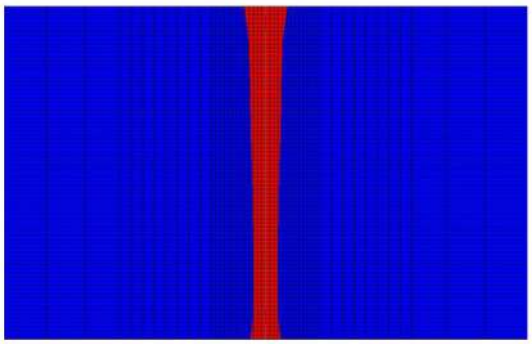

Figure 15: The calibrated molten zone in red.

The mechanical analysis is based on the momentum balance equation where inertial effects are neglected. The internal heating due to plastic dissipation is neglected considering the small strain rates generated by a welding operation. As this effect as well as the influence of stresses on metallurgical transformations is neglected, the mechanical analysis can be uncoupled from the thermo-metallurgical simulation. The computation is thus achieved in a second stage using the temperatures and phase proportions calculated previously. Heat transfer and microstructural evolution are considered in the mechanical analysis through four effects:

- the thermal strains.
- The influence of temperature and of the precipitate state evolution on the constitutive behavior (hard and soft proportions are state variables).
- The stress-strain relation must be temperature-dependent, and representative of the hard and soft material mixture.
- The nonlinear transient mechanical calculation is achieved using the temperature fields computed by a 3D Eulerian steady state thermal analysis as in [36].

5.1.1. FE results and comparison with experiments

To confront our modelling strategy to experiments a girth weld was done on a tubular structure of 40 mm thickness followed by a machining of 10 mm for the inner and outer surfaces. Then, residual stresses are obtained thanks to neutron diffraction measurements, according to the protocol of Wimpory *et al.* [37], along both the transversal and longitudinal directions and for several positions accross the weld (see orange arrow in Fig. 16). Some supplementary incremental Hole driling (iHD) data are extracted thanks to strain gauges located at the surface of the tube. In our industrial process the maximum heating rate in the HAZ is close to 160°C/s and the cooling velocity is close to 32°C/s between 500 and 150°C [38] . Consequently, this validation step is mandatory to check the consistency of our model since this later was calibrated thanks to isothermal treatments.[DB]

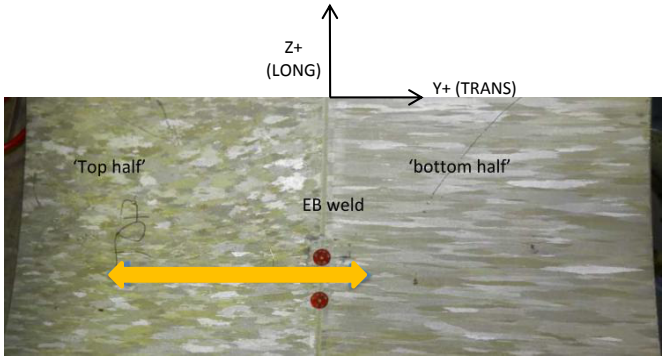

Figure 16: Representation of the girth weld, the line where the neutron diffraction experiments was performed is represented by an orange arrow, it is colinear to the transverse direction.

From a numerical point of view, the 3D thermal eulerian simulation is transformed into a temporal description on one section which is then used for the mechanical analysis. Indeed, as the structure is similar to a tube, a section perpendicular to the welding direction (Fig. 17a) is used with a relevant rotational symmetry conditions. The stresses are computed on this section after the welding operation (Fig. 17b), the inner and outer surfaces are substracted to the initial model to take into account machining (fig. 17c) and finally the stresses are balanced (Fig. 17d).

These simulation results are compared to neutron diffraction stress measurements at the inner and outer surfaces in Figs. 18 and 19: a very good correlation is observed. Furthermore, the good correlation between residual strains provided by strain gauges and simulations will validate the previous results (Fig. 20)

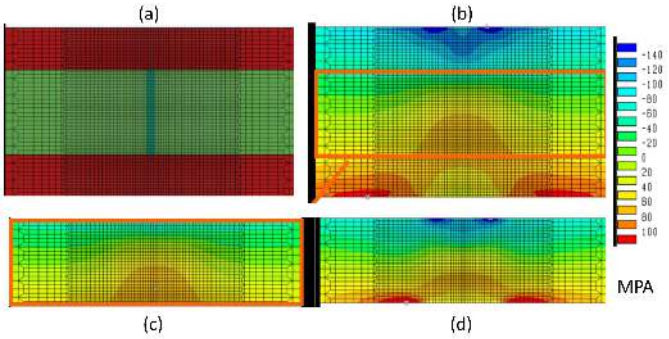

Figure 17: Transverse stresses (in the axial direction) before and after machining.

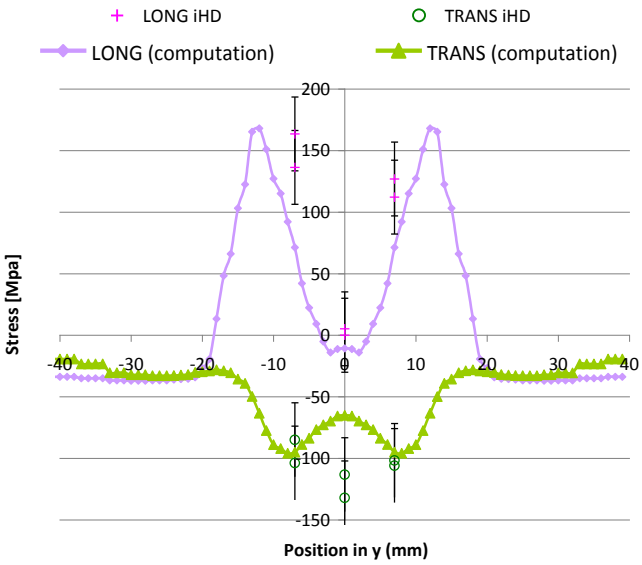

Figure 19: Comparison between iHD experiments and numerical simulation at outer surface (X=-10 mm).

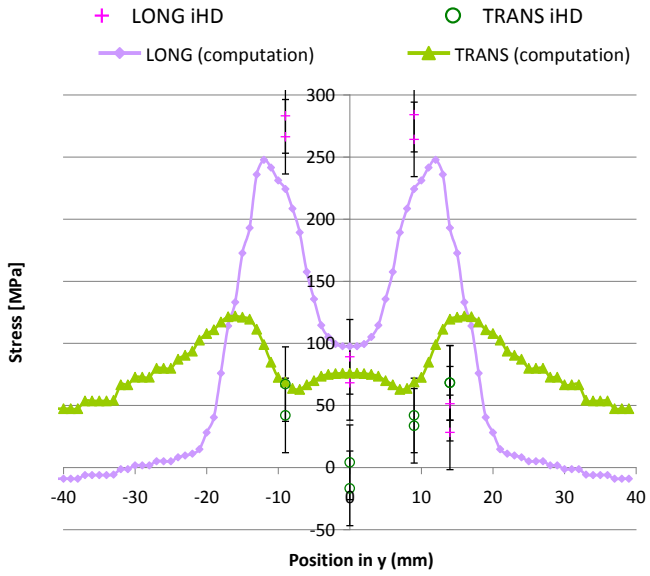

Figure 18: Comparison between iHD experiments and numerical simulation at inner surface (X=10 mm).

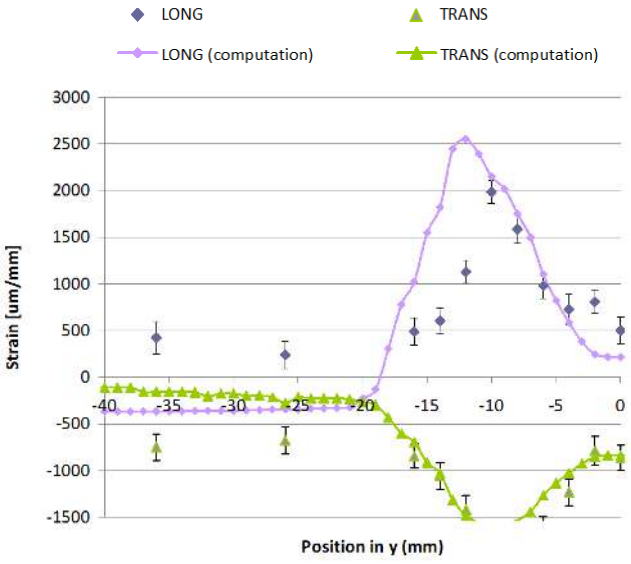

Figure 20: Comparison between neutrons diffraction (ND) experiments and numerical simulation (2 mm below the inner surface).

6. Conclusions

The mechanical behaviour of a 6061 age hardening alloy was investigated at medium and high temperature from T6 to O states. To be as representative as possible of the thermo-mechanical loading encountered during welding, no dwell time is used before the start of the tensile test.

The main experimental results are:

- from a T6 state, a softening is obtained at intermediate temperature (from 200 to 400° C) due to the dissolution and/or coarsening of the hardening precipitates during the tensile tests.
- The O state can be obtained, even thanks to a transient treatment, if the maximum temperature reaches at least $T = 500°$ C.

In a second part, a thermo-electrical model is used to reproduce the experimental tests from a T6 state. These FE simulations was coupled with a phenomenological microstructural-mechanical model proposed in this study. For this purpose, the stress-strain curves corresponding to the T6 and the O state (without microstructural evolution) have been identified by inverse method at all temperatures. Then, thanks to a mixture law and an isokinetic dissolution model, the resulting behaviour of the alloy can be reproduced for any heat treatments and then used for a welding thermal cycle simulation. It was shown that this kind of model can provide a good estimation of residual stresses for complex welding simulations.

7. Acknowledgements

The financial support of the CNRS through FEDERAMS, FR2145, is gratefully acknowledged as well as AREVA for the financial support. The authors wish to thank the TG7 (NeT) network and especially Robert Wimpory for ND measurements.

References

[1] A. Simar, Y. Bréchet, B. de Meester, A. Denquin, C. Gallais, T. Pardoen, Integrated modeling of friction stir welding of 6xxx series Al alloys: Process, microstructure and properties, Progress in materials science 57 (2012) 95–183.

[2] D. Bardel, M. Perez, D. Nelias, A. Deschamps, C. Hutchinson, D. Maisonnette, T. Chaise, J. Garnier, F. Bourlier, Coupled precipitation and yield strength modelling for non-isothermal treatments of a 6061 aluminium alloy, Acta Materialia 62 (2014) 129–140.

[3] D. Bardel, M. Perez, D. Nelias, S. Dancette, P. Chaudet, V. Massardier, Cyclic behaviour of a 6061 aluminium alloy: coupling precipitation and elastoplastic modelling, Acta Materialia 83 (2015) 256–268.

[4] A. Pickett, M. Fouinneteau, S. Gudgeon, V. Robin, J. Christlein, Model characterisation and failure analysis of welded aluminium components including process history, International Journal of Crashworthiness 12 (2007) 449–463.

[5] D. Smith, G. Zheng, P. Hurrell, C. Gill, B. Pellereau, K. Ayres, D. Goudar, E. Kingston, Measured and predicted residual stresses in thick section electron beam welded steels, International Journal of Pressure Vessels and Piping 120–121 (2014) 66–79.

[6] V. Robin, From the numerical modeling of manufacturing processes and welding in particular to the mechanical behavior of weldments, Ph.D. thesis, Ecole Nationale Suprieure des Mines de Saint-Etienne (2009).

[7] V. Robin, T. Pyttel, J. Christlein, A. Strating, Fracture analyses of welded components, Mathematical Modelling of Weld Phenomena 7 edited by H. Cerjak, H.K.D.H. Bhadeshia and E. Kozeschnik, Technische Universitt of Graz (2005) 519–535.

[8] O. Grong, H. Shercliff, Microstructural modelling in metals processing, Progress in materials science 47 (2002) 163–282.

[9] M. Zain-ul Abdein, D. Nélias, J. Jullien, F. Boitout, L. Dischert, X. Noe, Finite element analysis of metallurgical phase transformations in aa 6056-t4 and their effects upon the residual stress and distortion states of a laser welded t-joint, International Journal of Pressure Vessels and Piping 88 (6) (2011) 45–56.

[10] W. Yuan, R. Mishra, S. Webb, Y. Chen, B. Carlson, D. Herling, G. Grant, Effect of tool design and process parameters on properties of Al alloy 6016 friction stir spot welds, Journal of Materials Processing Technology 211 (2011) 972–977.

[11] X. Ren, L. Ruan, S. Yuan, H. Yang, Q. Zhan, L. Zheng, Y. Wang, F. Dai, Metallographic structure evolution of 6061-t651 aluminum alloy processed by laser shock peening: Effect of tempering at the elevated temperatures, Surface & Coatings Technology 221 (2013) 111–117.

[12] R. Ahmad, M. Bakar, Effect of a post-weld heat treatment on the mechanical and microstructure properties of aa6061 joints welded by the gas metal arc welding cold metal transfer method, Materials and Design 32 (2011) 5120–5126.

[13] D. Bardel, M. Fontaine, T. Chaise, M. Perez, D. Nelias, F. Bourlier, J. Garnier, Integrated modelling of a 6061-t6 weld joint: From microstructure to mechanical properties, Acta Materialia 117 (2016) 81–90.

[14] S. Abotula, V. Chalivendra, An experimental and numerical investigation of the static and dynamic constitutive behaviour of aluminium alloys, The Journal of Strain Analysis for Engineering Design 45 (8) (2010) 555–565.

[15] V. Robin, E. Feulvarch, J. Bergheau, 3d modelling of electro-magneto forming of metal sheets, Proceedings of the International Conference on Advances on Materials and Processing Technologies AMPT (2008) Bahrain.

[16] S. Andersen, H. Zandbergen, J. Jansen, C. Traeholt, U. Tundal, O. Reiso, The crystal structure of the β phase in Al-Mg-Si alloys, Acta Materialia 46 (9) (1998) 3283–3298.

[17] B. Milkereit, M. Starink, Quench sensitivity of al-mg-si alloys: A model for linear cooling and strengthening, Materials and Design 76 (2015) 117–129.

[18] T. Chanda, J. Zhou, J. Duszczyk, A comparative study on iso-speed extrusion and isothermal extrusion og 6061 Al alloy using 3D FEM simulation, Journal of Materials Processing Technology 114 (2001) 145–153.

[19] V. Massardier, T. Epicier, P. Merle, Correlation between the microstructural evolution of a 6061 aluminium alloy and the evolution of its thermoelectric power, Acta Materialia 48 (2000) 2911–2924.

[20] S. lan Li, Z. qi Huang, W. ping Chen, Z. ming Liu, W. jun Qi, Quench sensitivity of 6351 aluminum alloy, Transactions of Nonferrous Metals Society of China 23 (2013) 46–52.

[21] P. Bridgman, Stress distribution at the neck of tension specimen, Transactions of the American Society for Metals 32 (1944) 553–572.

[22] M. Zain-ul Abdein, D. Nélias, J. Jullien, A. Wagan, Thermo-Mechanical Characterisation of AA 6056-T4 and Estimation of its Material Properties using Genetic Algorithm, Materials & Design 31 (9) (2010) 4302–4311.

[23] R. Develay, Propriétés de l'aluminium et des alliages d'aluminium corroyés, Techniques de l'ingénieur MB5(M438) (1992) 1–21.

[24] S. Sharma, Effect of albite particles on the coefficient of thermal expansion behavior of the Al6061 alloy composites, Metallurgical and Materials Transactions A 31 (3) (2000) 773–780.

[25] O. Myhr, Ø. Grong, S. Andersen, Modelling of the age hardening behaviour of al-mg-si alloys, Acta Materialia 49 (1) (2001) 65–75.

[26] M. Nicolas, A. Deschamps, Characterisation and modelling of precipitate evolution in an Al-Zn-Mg alloy during non-isothermal heat treatments, Acta Materialia 51 (2003) 6077–6094.

[27] O. Myhr, Ø. Grong, Process modelling applied to 6082-T6 aluminium weldments. I: Reaction kinetics, Acta Metallurgica et Materialia 39 (11) (1991) 2693–2702.

[28] D. Maisonnette, M. Suery, D. Nélias, P. Chaudet, T. Epicier, Effects of heat treatments on the metallurgy and mechanical properties of a 6061 aluminum alloy, Materials Science & Engineering A 528 (2011) 2718–2724.

[29] ESI Group, Sysweld® 2005 Reference Manual (2005).

ACCEPTED MANUSCRIPT

[30] E. Feulvarch, V. Robin, J. Bergheau, Resistance spot welding simulation: a general finite element formulation of electrothermal contact conditions, Journal of Materials Processing Technology 153-154 (2004) 436–441.
[31] A. Hirose, K. Kobayashi, H. Yamaoka, N. Kurosawa, Evaluation of properties in laser welds of A6061-T6 aluminium alloy, Welding International 14 (6) (2000) 431–438.
[32] ASM, Properties of Wrought Aluminium and Aluminium Alloys., ASM Publication, 1990.
[33] Handbook, Metallic Materials and Elements for Aerospace Vehicle Structures, MIL-HDBK-5H, 1998.
[34] I. 1866, Numerical welding simulation, execution and documentation.
[35] M. Bergheau, R. Fortunier, Finite Element Simulation of Heat Transfer, iSTE Wiley Publishing, 2008.
[36] J. Bergheau, V. Robin, F. Boitout, Finite element simulation of processes involving moving heat sources application to welding and surface treatment, First International Conference on Thermal Process Modelling and Computer Simulation proceedings, Journal of Shanghai Jiaotong University 5 (2000) 114–122.
[37] R. Wimpory, M. Boin, Emphasizing the accuracy of the uncertainty of residual stress determination using neutron diffraction, Procedia Engineering 10 (2011) 1639–1644.
[38] D. Bardel, Role de la microstructure d'un alliage durcissement structural sur son comportement et sa tenue mcanique sous sollicitations cycliques aprs un transitoire thermique, Ph.D. thesis, INSA Lyon (2014).